

Lattice dynamics and vibrational spectra of the orthorhombic, tetragonal and cubic phases of methylammonium lead iodide

Federico Brivio,¹ Jarvist M. Frost,¹ Jonathan M. Skelton,¹ Adam J. Jackson,¹ Oliver J. Weber,¹ Mark T. Weller,¹ Alejandro R. Goñi,² Aurélien M. A. Leguy,³ Piers R. F. Barnes,³ and Aron Walsh^{1,4,*}

¹*Centre for Sustainable Chemical Technologies and Department of Chemistry, University of Bath, Claverton Down, Bath BA2 7AY, UK*

²*ICREA, Passeig Lluís Companys 23, E-08010 Barcelona,*

Spain; Institut de Ciència de Materials de Barcelona (ICMAB-CSIC), Campus UAB, E-08193 Bellaterra, Spain

³*Department of Physics, Imperial College London, SW7 2AZ, UK*

⁴*Global E3 Institute and Department of Materials Science and Engineering, Yonsei University, Seoul 120-749, Korea*

(Dated: September 24, 2015)

The hybrid halide perovskite $\text{CH}_3\text{NH}_3\text{PbI}_3$ exhibits a complex structural behaviour, with successive transitions between orthorhombic, tetragonal and cubic polymorphs at ca. 165 K and 327 K. Herein we report first-principles lattice dynamics (phonon spectrum) for each phase of $\text{CH}_3\text{NH}_3\text{PbI}_3$. The equilibrium structures compare well to solutions of temperature-dependent powder neutron diffraction. By following the normal modes we calculate infrared and Raman intensities of the vibrations, and compare them to the measurement of a single crystal where the Raman laser is controlled to avoid degradation of the sample. Despite a clear separation in energy between low frequency modes associated with the inorganic $(\text{PbI}_3)_n$ network and high-frequency modes of the organic CH_3NH_3^+ cation, significant coupling between them is found, which emphasises the interplay between molecular orientation and the corner-sharing octahedral networks in the structural transformations. Soft modes are found at the boundary of the Brillouin zone of the cubic phase, consistent with displacive instabilities and anharmonicity involving tilting of the PbI_6 octahedra around room temperature.

PACS numbers: 63.20.D, 63.20.Ry, 78.30.-j

I. INTRODUCTION

Materials that adopt the perovskite crystal structure are known for their complex structural landscapes, with a large number of accessible polymorphs depending on the temperature, pressure, and/or applied electric field. For ternary ABX_3 perovskites, the A site cation is at the centre of a cube formed of corner sharing BX_6 octahedra. Displacement of the A cation is usually associated with a ferroelectric (Brillouin zone centre) instability, while tilting of the BX_6 octahedral network is usually linked to antiferroelectric (Brillouin zone boundary) transitions.^{1,2}

Hybrid organic-inorganic perovskites are formed when one of the elemental perovskite building blocks is replaced by a molecular anion or cation.^{3,4} There exists a large family of such compounds, including the widely studied formate perovskites, which contain both molecular anions and cations.⁵⁻⁷ Hybrid *halide* perovskites are of current intense research effort, due to their high efficiency photovoltaic action.⁸⁻¹⁶

Methylammonium lead iodide (MAPbI_3 , where MA represents the CH_3NH_3^+ cation), was first reported by Weber in 1978.¹⁷ It is the most relevant hybrid halide perovskite for photovoltaic application. The transition from orthorhombic to tetragonal to cubic perovskite structures as a function of temperature has been studied by techniques including calorimetry and infrared spectroscopy¹⁸, single-crystal X-ray diffraction¹⁹, and dielectric spectroscopy.²⁰ Recently analysis of powder neutron diffraction (PND) measurements has provided more

quantitative insights into the temperature dependent behaviour of the MA cation within the anionic $(\text{PbI}_3)_n$ network.²¹ There is now direct evidence for the degree of order of the MA cation in the different phases, and the average lattice parameters (and thus extent of octahedral tilting) as a function of temperature through the first and second order phase transitions. Quasi-elastic neutron scattering has provided further insights into the rotational dynamics of the MA cation with a room temperature residence time of ~ 14 ps,²² while time-resolved vibrational spectroscopy identified fast librations (300 fs) and slow (3 ps) rotations of the molecule.²³

In this study, we calculate the phonon dispersion in each phase of MAPbI_3 within the harmonic approximation, computing the force constants with density functional theory (DFT). We use the PBEsol functional, which is a generalised-gradient-approximation (GGA) to the exchange-correlation functional, numerically evaluated with Perdew's method, adjusted to give more accurate lattice constants and forces for solids.²⁴ The lattice dynamic calculations allow the atomic origin of each phonon mode to be identified. Changes in lattice polarisation and polarisability for each eigenvector provide the infrared and Raman activity of each mode. Spectral features related to the inorganic and organic components (from 0 to 3000 cm^{-1}) are well reproduced in comparison to the Raman spectra of a single crystal of MAPbI_3 . Overlap is found between the vibrations of the CH_3NH_3^+ and PbI_3^- components up to 130 cm^{-1} , with the modes from 300 to 3000 cm^{-1} being associated with pure

molecular vibrations. The phonon dispersion has implications for developing quantitative models for the generation, transport and recombination of photo-generated electrons and holes in hybrid perovskite solar cells.

A. Structure Models

The normal modes of a system are defined for an equilibrium configuration. Calculating the vibrations for a non-equilibrium structure will result in imaginary frequencies upon diagonalising the dynamical matrix. Therefore we have generated well optimised structures of MAPbI₃. One challenge in calculating the phonons of hybrid perovskites is the soft nature and complicated potential energy landscape of some of the restoring potentials, particularly those involving the organic cation.

The models for the crystal structures used in this study are discussed in detail below and a comparison with the measured diffraction patterns are provided as Supplementary Material.²⁵

1. Orthorhombic Phase

The orthorhombic perovskite structure is the low temperature ground state of MAPbI₃ and maintains its stability up to ca. 165 K.^{21,26,27} A comparison of the enthalpy from DFT calculations confirms this ordering in stability. The difference in enthalpy is small, just 2 meV per MAPbI₃ unit compared to the most stable tetragonal phase, yet 90 meV compared to the high-temperature cubic phase.

Initial diffraction pattern solutions assigned the *Pna2*₁ space group.^{18,26} Recent analysis of higher quality powder neutron diffraction data reassigns it to *Pnma* (a *D*_{2h} point group).²¹ The structure is a $\sqrt{2}a \times \sqrt{2}a \times 2a$ supercell expansion of the simple cubic perovskite lattice, i.e. following the lattice transformation matrix

$$\begin{pmatrix} 1 & -1 & 0 \\ 1 & 1 & 0 \\ 0 & 0 & 2 \end{pmatrix}. \quad (1)$$

In the *Pna2*₁ phase, the PbI₆ octahedra are distorted and tilt as $a^+b^-b^-$ in Glazer notation¹ with respect to the orientation of the conventional cubic cell. In this low-temperature phase, the four molecular cations in the unit cell are static on the diagonals of the *ab* planes pointing towards the undistorted facets of the cuboctahedral cavity. Correspondingly, molecules belonging to different planes are anti-aligned with a head-tail motif. Such an antiferroelectric alignment is expected from consideration of the molecular dipole-dipole interaction.²⁸

In the low temperature orthorhombic phase the CH₃NH₃⁺ sublattice is fully ordered (a low entropy state). The ordering may be sensitive to the material preparation and / or cooling rate into this phase, i.e. the degree

of quasi-thermal equilibrium. It is possible that different ordering might be frozen into the low temperature phase by epitaxy or application of external force or electric fields.

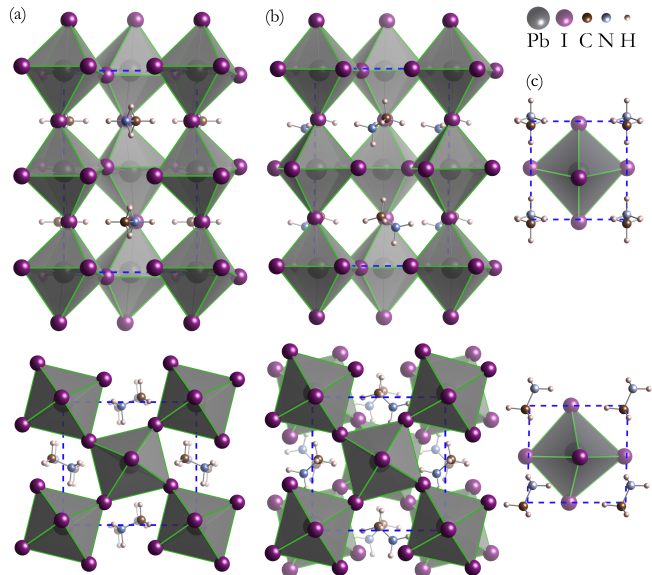


FIG. 1. (Color online) The crystal structures of the (a) orthorhombic, (b) tetragonal and (c) cubic phases of CH₃NH₃PbI₃. The upper and lower panels are oriented through $\langle 100 \rangle$ and $\langle 001 \rangle$, respectively. Lattice parameters and coordinates obtained from powder neutron diffraction were optimised using density functional theory (PBEsol). The PbI₆ octahedra are shaded grey. All structures are available in an on-line repository.²⁹

2. Tetragonal Phase

At 165 K MAPbI₃ goes through a first-order phase transition from the orthorhombic to the tetragonal space group *I4/mcm* (*D*_{4h} point group), which continuously undergoes a second-order phase transition to the cubic phase by ca. 327 K^{21,26,27}. As with the orthorhombic phase, this can be considered a $\sqrt{2}a \times \sqrt{2}a \times 2a$ expansion of the cubic perovskite unit cell.

The molecular cations are no longer in a fixed position as in the orthorhombic phase. The molecules are disordered between two non-equivalent positions in each cage.^{27,30} The tetragonal distortion parameter in the cubic basis is greater than unity ($\frac{c}{2a} \sim 1.01$ at 300 K), corresponding to an elongation of the PbI₆ octahedra along the *c* axis. The associated octahedral tilting pattern is $a^0a^0c^-$ in Glazer notation.

Atomistic simulations within periodic boundary conditions require an ordered configuration. The solved crystal structure shows that there are several possible configurations for the organic cations within the tetragonal unit cell. These configurations have similar enthalpies

Phase	a (Å)	b (Å)	c (Å)	$d(\text{Pb-I})$ (Å)	Z	Cut-off (eV)	k -points	Forces (meV/Å)	ΔH (meV)
<i>Orthorhombic</i>									
DFT/PBEsol	9.04	12.66	8.35	3.18	4	700	$5 \times 4 \times 5$	1	0
PND (100 K)	8.87	12.63	8.58	3.19					
<i>Tetragonal</i>									
DFT/PBEsol	8.70	8.72	12.83	3.19	4	800	$5 \times 5 \times 3$	1	2
PND (180 K)	8.81	8.81	12.71	3.17					
<i>Cubic</i>									
DFT/PBEsol	6.29	6.23	6.37	3.17	1	700	$6 \times 6 \times 6$	1	90
PND (352 K)	6.32	6.32	6.32	3.16					

TABLE I. Equilibrium cell parameters from DFT/PBEsol energy minimisation, including the converged plane-wave cut-off, k -point mesh and force threshold. Z represents the number of formula units of $\text{CH}_3\text{NH}_3\text{PbI}_3$ per cell. The calculated difference in enthalpy (ΔH) of each phase is given with respect to the ground-state orthorhombic configuration and per $\text{CH}_3\text{NH}_3\text{PbI}_3$ unit. Shown for comparison are the cell parameters and average Pb-I inter-atomic separations (d) from powder neutron diffraction (PND).²¹

within DFT,³¹ which is consistent with the observed disorder. We choose to use the most energetically stable structure, which is also consistent with a previous DFT investigation.³²

In the model of the tetragonal structure, the MA cations are aligned as in the orthorhombic phase, towards the face of the perovskite cage, i.e. $\langle 100 \rangle$ in the cubic basis. The MA in different (001) planes are approximately orthogonal to one other. The orientational dynamics of the methylammonium ions, which exists above 165 K, is not taken into account in this equilibrium configuration study.

3. Cubic Phase

With increasing temperature the tetragonal lattice parameters become more isotropic (i.e. $\frac{c}{2a}$ moves closer to 1), and the molecular disorder increases, to the point where a transition to a cubic phase occurs around 327 K. The transition can be seen clearly from changes in the heat capacity,¹⁸ as well as in temperature dependent neutron diffraction²¹.

The cubic space group $Pm\bar{3}m$ (O_h symmetry) has been assigned to this high-temperature phase. Although the methylammonium ions possess C_{3v} symmetry, the orientational disorder gives rise to the effective higher symmetry on average. The local structure will necessarily have a lower symmetry. Indeed, for the bromide and chloride analogues of MAPbI_3 , pair-distribution function analysis of X-ray scattering data indicates a local structure with significant distortion of the lead halide framework at room temperature.³³

We previously considered alignment of the molecules along the principal $\langle 100 \rangle$ (face), $\langle 110 \rangle$ (edge), and $\langle 111 \rangle$ (diagonal) directions of the cubic unit cell, and showed that they are of similar DFT enthalpy, with a small barrier for rotation.³⁴ Further *ab-initio* molecular dynamics showed an average preference for the $\langle 100 \rangle$ facial configuration at 300 K.²⁸ Therefore we chose the $\langle 100 \rangle$ configuration as our reference structure for the

lattice vibrations.

Representations of the crystal structure of each phase are shown in Figure 1, the equilibrium structure parameters are listed in Table I, and the structures themselves are available in an on-line repository.²⁹

II. METHODS

A. Computational

The total energy and atomic forces were computed from first-principles within density functional theory as implemented in the code VASP.^{36,37} Noise in the lattice vibrations was minimised by rigorous convergence of total Kohn-Sham energy with respect to the basis set (kinetic energy cut-off for plane waves) and sampling of reciprocal space (density of the k -point mesh). The final computational set-up is summarised in Table I.

We performed complete optimisation of the cell volume, shape and atomic positions, with the PBEsol²⁴ semi-local exchange-correlation functional. The scalar-relativistic projector-augmented wave method³⁸ was employed, with a pseudo-potential treating the Pb 5d orbitals as valence. Spin-orbit coupling was not considered as it mainly affects the Pb 6p conduction band, which does not influence the interatomic interactions at equilibrium. All atomic forces were reduced to below a threshold of 1 meV/Å. Due to the presence of the organic cations, which breaks the ideal lattice symmetry, deviations in the expected parameters can occur, e.g. in the high temperature pseudo-cubic phase, the three equilibrium lattice parameters are not equal. The equilibrium structure parameters (at 0 K and excluding zero-point contributions) are reported in Table I.

The normal modes are calculated within the harmonic approximation, using the Phonopy³⁹⁻⁴¹ package to construct and evaluate the dynamical matrix composed of DFT force constants. Both the finite displacement method (FDM or supercell approach)⁴² and density functional perturbation theory (DFPT)⁴³ approaches to

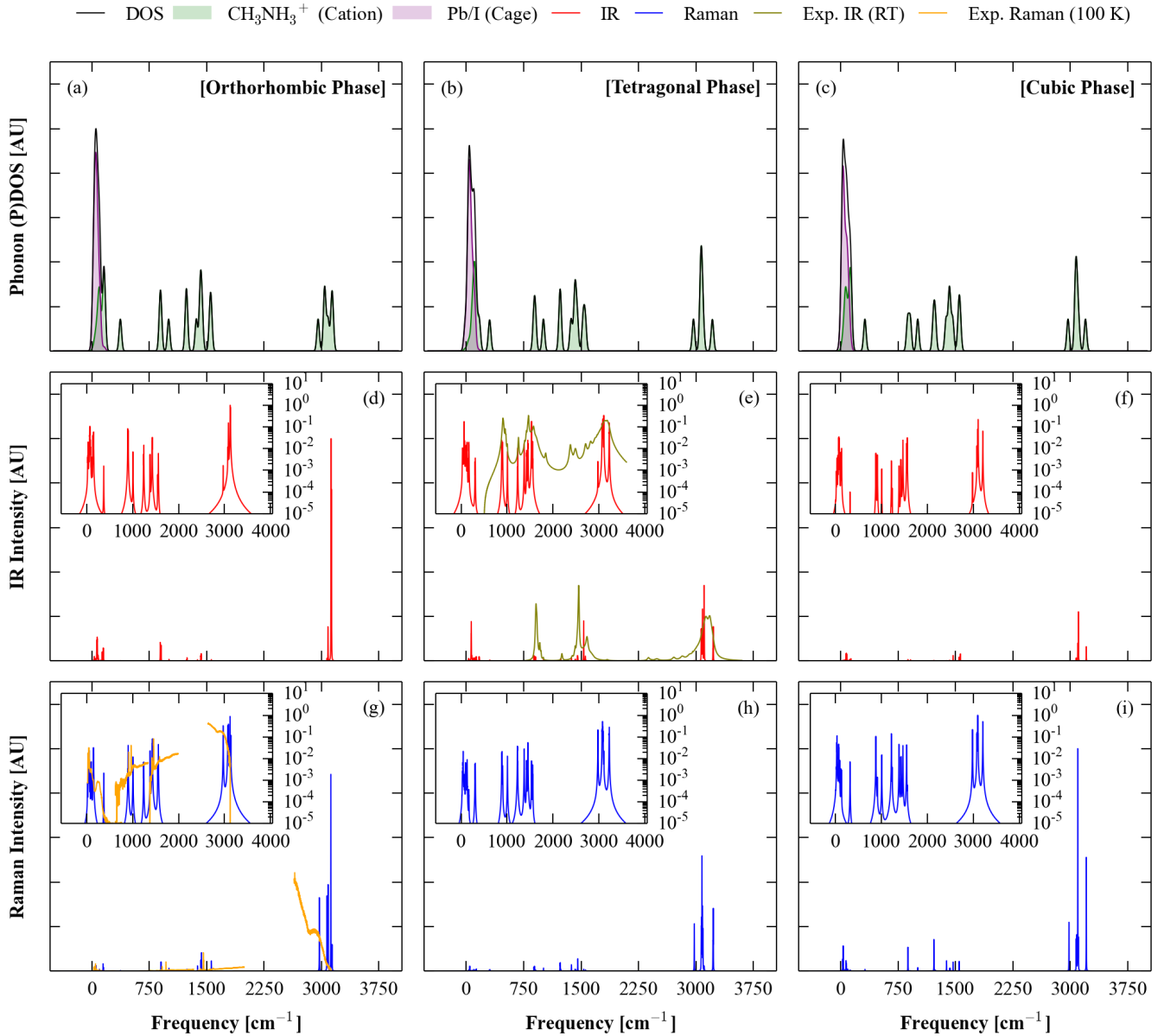


FIG. 2. (Color online) (a-c) Projected phonon density of states (PDOS) for the three phases of $\text{CH}_3\text{NH}_3\text{PbI}_3$ as calculated from DFT/PBESol, generated by convolution with a 32 cm^{-1} Lorentzian. Note that no imaginary (negative) modes are found in the orthorhombic or tetragonal phases. (d-f) Simulated infrared (IR) spectra. (e) The measured IR spectrum at 300 K from Ref. 35 is coplotted in mustard (light grey). (g-i) Simulated Raman spectrum. (g) The measured Raman spectrum of a single crystal in the orthorhombic phase at 100 K is coplotted in orange (light grey). Simulated spectra were broadened by convolution of a 2 cm^{-1} Lorentzian. Insets in the simulated spectra are the same data on a logarithmic scale to show the structure in the low intensity modes.

construct the force constants were tested. The results of both approaches produced similar vibrational spectra, with a variance in the mode energies of 6 cm^{-1} .

Within a primitive cell of N atoms there are $6N$ possible displacements ($\pm x, \pm y, \pm z$), which can be reduced by the crystal symmetry. For the orthorhombic phase, the 288 possible displacements are reduced to 41, while the tetragonal and cubic phases required 288 and 72 displacements, respectively. The phonon dispersion (for \mathbf{q} -points

away from the Brillouin zone centre, the Γ point) in the cubic phase was probed in a $2 \times 2 \times 2$ supercell. Due to computational expense, we do not calculate this for the other (larger unit cell) phases. For the phonon density of states, Brillouin-zone integrations were performed with $36 \times 36 \times 36$ (orthorhombic and tetragonal) and $48 \times 48 \times 48$ (cubic) Γ -centered Monkhorst-Pack q -meshes.

Once the normal eigenmodes and eigenvalues are calculated, it is possible to model their associated Raman and

infrared (IR) activity by mode following. The two spectroscopic techniques probe different physical responses of the material: the change in polarisation for IR and the change in polarisability for Raman. The IR spectra are simulated with the analytic formula of Gianozzi & Baroni (using the Born effective charge tensor)⁴³. Prediction of the Raman spectra required computing the change in macroscopic dielectric tensor with respect to each normal mode of the system, a significant DFT calculation in terms of computational expense.⁴⁴

B. Experimental

Methylammonium lead iodide single crystals were grown according to the method of Poglitsch and Weber.²⁶ 12.5 g of lead acetate trihydrate ($\text{Pb}(\text{CH}_3\text{CO}_2)_2 \cdot 3\text{H}_2\text{O}$, Sigma) was dissolved in 10 mL hydroiodic acid (HI_{aq} , 57 wt%, Sigma) in a 50 mL round bottom flask and heated to 100°C in an oil bath. Separately, 0.597 g of CH_3NH_2 (aq, 40 wt%, Sigma) was added dropwise to a further 2 mL of HI_{aq} kept at 0°C in an ice bath under stirring. The methylammonium iodide solution was then added to the lead acetate solution and the mixture was cooled over five days to a temperature of 46°C, resulting in the formation of black crystals with largest face length around 8 mm. The content of the flasks was subsequently filtered and dried for 12 hours at 100°C.

Raman spectra were collected in backscattering geometry with a high resolution LabRam HR800 spectrometer using a grating with 600 lines per millimetre and equipped with a liquid-nitrogen-cooled charge coupled device (CCD) detector. The 785 nm line of a diode-pumped solid state laser was used as excitation beam and focused onto the sample using a long distance 20× microscope objective. Raman measurements were carried out at 100 K using a gas-flow-type cryostat with optical access that fits under the microscope of the Raman setup. The high spectral resolution and stray-light rejection of the LabRam spectrometer, particularly in combination with the 785 nm line, allowed us to measure the Raman spectrum of MAPI at very low Raman shifts down to 20 to 30 cm^{-1} . This way and for the first time, we were able to spectrally resolve several low-frequency modes associated to vibrations of the inorganic cage of the hybrid perovskite.

Heating by laser light directly absorbed by $\text{CH}_3\text{NH}_3\text{PbI}_3$ has been shown to lead to rapid degradation of the material resulting in PbI_2 Raman signatures.⁴⁵ Since 785 nm light is only weakly absorbed the heating effect of the laser was low enough to ensure the crystal structure was preserved. The power density incident on the sample was kept at 80 W/cm^2 . At such power level, it was checked that no appreciable spectral changes in peak width and/or position occurred, yet maintaining a good signal-to-noise ratio. Further, samples were kept under vacuum inside the cryostat during the measurements.

III. RESULTS

A. Harmonic Phonons

The full phonon density of states (DOS) is shown for the three phases of $\text{CH}_3\text{NH}_3\text{PbI}_3$ in Figure 2. Also plotted is the partial DOS, where assignment to CH_3NH_3^+ or PbI_3 is performed based on the atomic contribution to each eigenvector. An animation of all 36 eigenmodes of the cubic phase is provided as Supplementary Material²⁵.

Qualitatively, each MAPbI_3 phase shows similar vibrational properties with three energetic regions of phonons: (i) a low-frequency band from 0–150 cm^{-1} ; (ii) a mid-frequency band from 280–1600 cm^{-1} ; (iii) a high-frequency band from 2900–3300 cm^{-1} . These ranges are consistent with previous computational reports.^{46,47}

Due to the large difference in atomic mass of the organic and inorganic components, and to the difference in bonding between the inorganic cage and the covalently bonded molecule, we anticipated that the low frequency modes would comprise entirely of motion by the PbI_6 octahedra, while the high frequency modes will involve the CH_3NH_3^+ cation. This is qualitatively the case, but there is also significant coupling between the two. Taking the example of the cubic phase with 36 modes: the highest-energy 18 modes (forming bands ii and iii) correspond to molecular vibrations, i.e. the $3N-6$ modes of the methylammonium ion. For an isolated non-linear molecule, the 6 translational and rotational degrees of freedom do not contribute to the pure vibrational spectrum, but this is not the case for a molecule inside a cuboctahedral cavity.

The 6 additional molecular modes are strongly coupled to the 9 modes (i.e. $3N-3$ for PbI_3) associated with stretching of the Pb–I bonds and breathing of the PbI_6 octahedra, which results in the spectral overlap observed in the partial DOS of band i. Particularly striking is the low-frequency pivoting motion associated with the libration of the molecular dipole, coupled with a breathing of the octahedral framework (e.g. modes 10 and 15 in the SI). The final three zero-frequency modes correspond to acoustic translations of the lattice.

B. Vibrational Spectra

For MAPbI_3 it is not possible for the relaxed (non-idealised) crystal structures to assign the spectral activity directly with group theoretic irreducible representation analysis of the phonon modes. The molecule breaks the average crystal symmetry. This symmetry lowering allows for simultaneous Raman and IR activity even in the pseudo-cubic phase. The predicted spectra (the Γ point phonon modes weighted by the computed spectral intensity, convolved with a Lorentzian for experimental comparison) are reported in Figure 2 for each phase.

Raman and IR activity is observed across each of the three phonon bands previously discussed. A notable exception is the lowest-energy purely molecular vibration

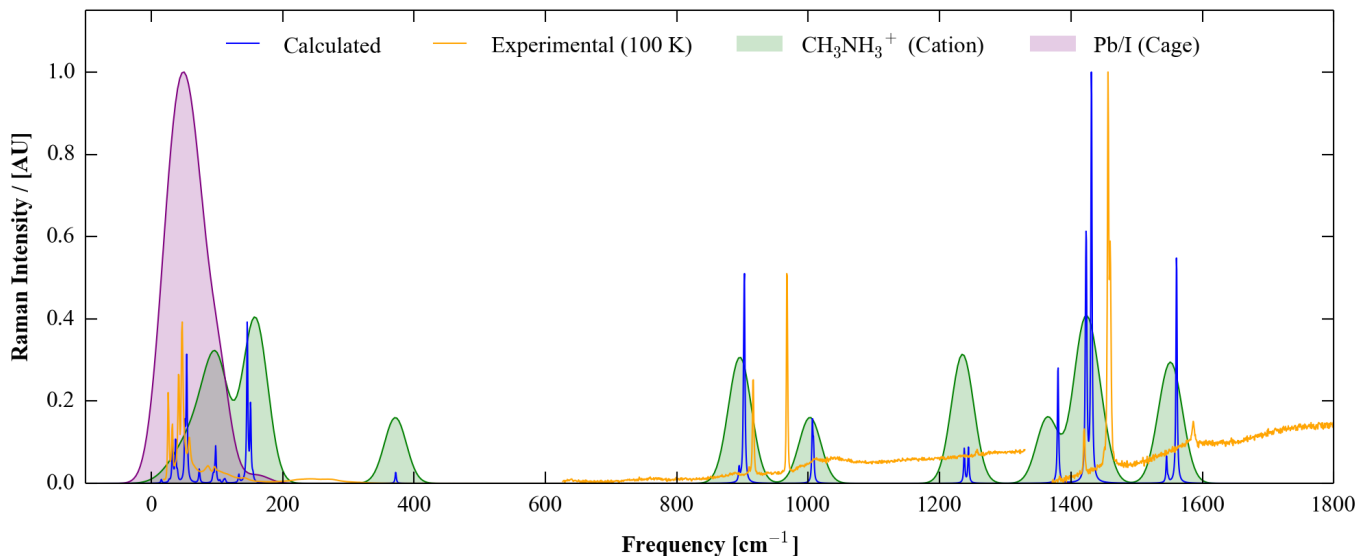


FIG. 3. (Color online) Comparison of the calculated and measured (100 K) Raman spectrum for the orthorhombic perovskite phase of $\text{CH}_3\text{NH}_3\text{PbI}_3$ in the range $0\text{--}1800\text{ cm}^{-1}$, which includes phonon modes centred on the inorganic cage (lowest frequency), organic cage (highest frequency) and coupled-modes (intermediate frequency). The simulated spectrum was broadened by convolving a 2 cm^{-1} Lorentzian (to match experimental broadening of the high resolution Raman spectrometer), while the underlying phonon density of states is shown for comparison with a broadening of 0.5 THz .

near 300 cm^{-1} , which is neither Raman nor IR active.

To understand the effect of embedding the methylammonium in MAPbI_3 , we calculate the normal mode vibrations of an isolated methylammonium ion in vacuum with a similar density functional theory method to our periodic calculations (PBE with an atom centered augmented cc-pVQZ basis set). Thereby we calculate the 18 molecular modes, directly accessing their symmetries and nature. The C_{3v} symmetry of the molecule separates the vibrational bands into one A symmetric mode and blue-shifted two-fold degenerate asymmetric E modes. The six bands we find are in ascending energy: twist around the C–N axis ($282, 886\text{ cm}^{-1}$); vibration along the C–N axis ($923, 1239\text{ cm}^{-1}$); bending of the C–H bonds ($1418, 1451\text{ cm}^{-1}$); bending of the N–H bonds ($1478, 1622\text{ cm}^{-1}$); stretching of the C–H bonds ($3018, 3119\text{ cm}^{-1}$); stretching of the N–H bonds ($3321, 3395\text{ cm}^{-1}$).

As the cation charge density is centred towards the N, the motion of the protons associated with N have the strongest affect on the dipole moment and therefore strongest IR activity. Due to the stronger bonds, their frequencies are consistently blue shifted relative to the C end. Owing to the molecular dipole moment (2.2 D ,²⁸ which is rotation and position invariant, and corresponds to a polarisation contribution of $\sim 3\text{ }\mu\text{C}/\text{cm}^2$), the two high-frequency asymmetric stretching modes of NH_3^+ (band **iii**) results in the strongest absolute IR intensity. The hydrogen stretching modes (band **iii**) are responsible for significant Raman activity. The only mode involving C or N motion is the weakly IR and Raman active vibration at 923 cm^{-1} (vacuum), 1007 cm^{-1} (cubic perovskite).

The rotation of the CH_3 against the NH_3 unit, while being strongly populated in molecular dynamic simulations, and which forms the main source of quasi-elastic neutron scattering, is entirely IR and Raman inactive in vacuum. This is the mode responsible for the 282 cm^{-1} (vacuum), 318 cm^{-1} (cubic), $300\text{--}310\text{ cm}^{-1}$ (tetragonal), $370\text{--}372\text{ cm}^{-1}$ (orthorhombic) vibration. Progressive confinement of MA from vacuum to the orthorhombic phase blue-shifts the energy of the vibration.

In the solid state, the degeneracies in the molecular modes are typically split by local environment effects, peaks are both redshifted and blue-shifted, and the IR and Raman activity varies. As such, it is evident that analysis of the Raman and IR spectra in the experimentally easily accessible molecular frequency range can enable statements to be made about the local structure and configuration of the hybrid perovskite. Our data is collected for a particular representation of the cubic and tetragonal phase; in reality the location of the MA in these phases will be disordered. As such, detailed comparison of theory to experiment will require sampling the thermodynamic ensemble of structures.

To our knowledge, no Raman spectra for the three phases have previously been reported across the full frequency range. The spectrum up to 450 cm^{-1} was reported in Ref. 46. Reliable measurements are a challenge due to chemical instability of the material. MAPbI_3 is strongly affected by environmental conditions, such as the presence of ambient moisture^{27,48}. Isolated in vacuum the material can still decompose and bleach due to heating, including by that imposed by the (typically

high) Raman laser fluence.⁴⁵ Such degradation leads to the formation of PbI_2 , which overlaps in Raman spectra with MAPbI_3 , and so easily leads to misinterpretation.

The Raman spectra of a high-quality single crystal of MAPbI_3 is shown in Figure 2, and compared in detail with the calculations in Figure 3. Across the full spectral range, the agreement between the predicted and measured spectra is good, with the response across bands **i**, **ii** and **iii** well reproduced. On closer inspection in Figure 3, there are noticeable shifts in peak positions, which can be attributed to three potential sources of error: (a) the harmonic approximation (anharmonic renormalisation may be large); (b) the limits of the exchange-correlation treatment (non-local interactions may be important); (c) the assumption of a fully-ordered structure (local inhomogeneity may be prevalent). There is also a notable case of a missing peak around 150 cm^{-1} , which we can tentatively attribute to a lifetime broadening effect. The same level of theory applied to the lead based semiconductors PbS and PbTe results in quantitative agreement with measured phonon frequencies and dispersion,⁴⁹ which highlights the complex nature of $\text{CH}_3\text{NH}_3\text{PbI}_3$.

We have also included in Figure 2 a room temperature IR spectrum reported by Glaser et al.³⁵, which again shows excellent agreement across the spectrum. A number of very weak absorption peaks below 3000 cm^{-1} are evident, which could be related to molecular disorder and/or partial decomposition. The temperature resolved (between 140 and 299 K) IR spectra for tetragonal and orthorhombic phases have been previously reported by Yamamuro⁵⁰. We reproduce the position and the intensity of the peak observed at 900 cm^{-1} , reliably assigning it to the (also Raman active) C–N bond stretch. High quality IR measurements, in particular looking at the very low energy transitions, would provide considerable information on the nature of the domains and local structure in a MAPbI_3 film.

C. Anharmonic Effects

The lattice dynamic simulations discussed above were performed within the harmonic approximation. All eigenmodes at the centre of the Brillouin zone were real (positive frequencies) for each phase, *i.e.* the structures are locally stable.

The phonon dispersion across the first Brillouin zone is shown for the cubic perovskite structure in Figure 4. Here imaginary (negative frequency or ‘soft’) modes are found at the zone boundaries. Such instabilities are a common feature of the perovskite structure, and represent antiferroelectric distortions linked to rotations and tilting of the octahedra in neighbouring unit cells.² The soft modes are centred around the R and M points, which correspond to the $\langle 111 \rangle$ and $\langle 110 \rangle$ directions in the cubic lattice. This behaviour is similar to the inorganic perovskite CsPbCl_3 , where neutron scattering was used to probe condensation of these modes,

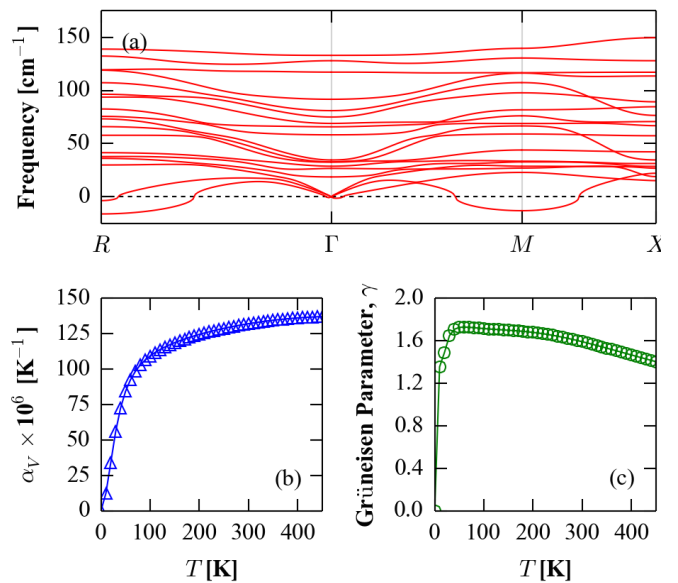


FIG. 4. (Color online) Vibrational properties of the cubic phase of MAPbI_3 : (a) Phonon dispersion of the low frequency (inorganic cage) modes within the harmonic approximation. Negative frequency (imaginary or ‘soft’) modes are found at the Brillouin zone boundary points M ($\frac{2\pi}{a}(\frac{1}{2}, \frac{1}{2}, 0)$) and R ($\frac{2\pi}{a}(\frac{1}{2}, \frac{1}{2}, \frac{1}{2})$). (b) Volumetric thermal expansion within the quasi-harmonic approximation. (c) Average Grüneisen parameter within the quasi-harmonic approximation.

which leads to successive transitions from the cubic to tetragonal to orthorhombic phases.⁵¹ The effect of these modes in MAPbI_3 , and the associated high levels of anharmonicity at room temperature can be observed directly in molecular dynamics simulations, where temporal rotations of the CH_3NH_3^+ ions and distortions of the PbI_6 octahedra have been found in several studies.^{22,28,52}

An approach to including the effects of temperature (thermal expansion) and first-order anharmonicity in lattice dynamic calculations is the quasi-harmonic approximation (QHA).^{53,54} The computational cost is one order of magnitude higher than the harmonic approximation and thus was considered for the cubic phase only. The volumetric thermal expansion coefficient extracted from the PND data at 300 K is $1.32 \times 10^{-4}/\text{K}$, which compares very well to the value of $1.25 \times 10^{-4}/\text{K}$ computed within the QHA. The predicted thermal expansion for MAPbI_3 is similar to inorganic semiconductors (e.g. for PbTe the value is $0.7 \times 10^{-4}/\text{K}$ at 300 K⁴⁰) and positive over the full temperature range.

The temperature dependence of the phonon modes can be described by the Grüneisen parameter, which has an average of around 1.6 (see Figure 4), slightly below the value of 1.7 found in PbI_2 ⁵⁵. The imaginary modes at R and M remain at all temperatures, consistent with the cubic lattice being a dynamic average of a locally distorted structure; the same phenomenon is observed in CsSnI_3 .⁵⁶ The high level of anharmonicity associated with the soft tilting modes is consistent with

the ‘ultra low’ ($< 1 \text{ Wm}^{-1}\text{K}^{-1}$ at 300 K) lattice thermal conductivity reported for single crystals and polycrystalline MAPbI_3 .⁵⁷ Hybrid halide perovskites are thus also promising for application in thermoelectric devices if thermal stability issues can be overcome.⁵⁸

IV. CONCLUSIONS

The vibrational frequencies of three crystallographic phases of the hybrid perovskite $\text{CH}_3\text{NH}_3\text{PbI}_3$ have been investigated. We identified three main phonon branches present in the three phases. Two high-frequency branches are associated with the vibration and bond stretching of the molecular cation with frequencies in the range 300 cm^{-1} to 3300 cm^{-1} . The lowest energy branch, below 150 cm^{-1} , arises predominately from the inorganic cage, but with half the modes coupled to the motion of the molecule. The simulated Raman spectrum is in good agreement with measurements on a single crystal of MAPbI_3 . Dynamic instabilities occur at the zone boundaries, which requires methods beyond the harmonic approximation, such as self-consistent phonon theory, for an accurate treatment. These results suggest that the room temperature structure of MAPbI_3 is fluctuational, owing to the persistent tilting and distortion of the octahedral networks and rotations of the molecular cations.

These factors may be important for developing a quantitative understanding and model of how hybrid perovskite solar cells operate. Upon excitation, the relative stability of free carriers and excitons depends intimately on the dielectric screening of the material, which includes vibrational and rotational components. The transport and recombination of photo-generated charge

carriers will also be influenced by electron-phonon coupling, which can significantly reduce the effective size and distribution of electrons and holes within the perovskite layer.

V. WEB ENHANCED

An animation of the 36 Γ -point phonon modes of the cubic phase of MAPbI_3 in gif format is available at http://people.bath.ac.uk/aw558/temp/mapi_phonon.gif.

ACKNOWLEDGMENTS

The authors are grateful for helpful discussions with Mariano Campoy-Quiles. The research at Bath has been supported by the EPSRC (Grant No. EP/K016288/1 and EP/M009580/1), the ERC (Grant No. 277757), EU-FP7 (Grant No. 316494), and the Royal Society. AJJ and OJW were funded through the CDT in Sustainable Chemical Technologies (EPSRC Grant No. EP/G03768X/1). PRFB and AMAL are grateful to the EPSRC (Grant Nos. EP/J002305/1, EP/M014797/1, and EP/M023532/1). ARG acknowledges the Spanish Ministerio de Economía y Competitividad (MINECO) through project number MAT2012-37776 and CSD2010-00044 (Consolider NANOTHERM). This work benefited from access to both the University of Bath’s High Performance Computing Facility and ARCHER, the UK’s national high-performance computing service, which is funded by the Office of Science and Technology through EPSRC’s High End Computing Programme (Grant No. EP/L000202).

* a.walsh@bath.ac.uk

¹ A. M. Glazer, *Acta Crystallogr. Sect. B* **28**, 3384 (1972).
² N. A. Benedek and C. J. Fennie, *J. Phys. Chem. C* **117**, 13339 (2013).
³ D. B. Mitzi, *J. Chem. Soc. Dalt. Trans.* **2001**, 1 (2001).
⁴ J. M. Frost, K. T. Butler, F. Brivio, C. H. Hendon, M. Van Schilfgaarde, and A. Walsh, *Nano Lett.* **14**, 2584 (2014), arXiv:1402.4980.
⁵ A. B. Cairns and A. L. Goodwin, *Chem. Soc. Rev.* **42**, 4881 (2013).
⁶ W. Li, Z. Zhang, E. G. Bithell, A. S. Batsanov, P. T. Barton, P. J. Saines, P. Jain, C. J. Howard, M. A. Carpenter, and A. K. Cheetham, *Acta Mater.* **61**, 4928 (2013).
⁷ G. Kieslich, S. Kumagai, K. T. Butler, T. Okamura, C. H. Hendon, S. Sun, M. Yamashita, A. Walsh, and A. K. Cheetham, *Chem. Commun.*, Advance Article (2015).
⁸ A. Kojima, K. Teshima, Y. Shirai, and T. Miyasaka, *J. Am. Chem. Soc.* **131**, 6050 (2009).
⁹ J.-H. Im, C.-R. Lee, J.-W. Lee, S.-W. Park, and N.-G. Park, *Nanoscale* **3**, 4088 (2011).

¹⁰ M. M. Lee, J. Teuscher, T. Miyasaka, T. N. Murakami, and H. J. Snaith, *Science* (80-.). **338**, 643 (2012).
¹¹ M. Liu, M. B. Johnston, and H. J. Snaith, *Nature* **501**, 395 (2013).
¹² F. De Angelis, *Acc. Chem. Res.* **47**, 3349 (2014).
¹³ J. Even, L. Pedesseau, C. Katan, M. Kepenekian, J.-S. Lauret, D. Saponi, and E. Deleporte, *J. Phys. Chem. C* **119**, 10161 (2015).
¹⁴ A. Walsh, D. O. Scanlon, S. Chen, X. G. Gong, and S.-H. Wei, *Angew. Chemie Int. Ed.* **54**, 1791 (2015), arXiv:1411.7606.
¹⁵ A. Walsh, *J. Phys. Chem. C* **119**, 5755 (2015).
¹⁶ N. J. Jeon, J. H. Noh, W. S. Yang, Y. C. Kim, S. Ryu, J. Seo, and S. I. Seok, *Nature* **517**, 476 (2015).
¹⁷ D. Weber, *Zeitschrift für Naturforsch. B* **33b**, 1443 (1978).
¹⁸ N. Onoda-Yamamuro, T. Matsuo, and H. Suga, *J. Phys. Chem. Solids* **51**, 1383 (1990).
¹⁹ Y. Kawamura, H. Mashiyama, and K. Hasebe, *J. Phys. Soc. Japan* **71**, 1694 (2002).
²⁰ N. Onoda-Yamamuro, T. Matsuo, and H. Suga, *J. Phys. Chem. Solids* **53**, 935 (1992).

- ²¹ M. T. Weller, O. J. Weber, P. F. Henry, A. M. Di Pumpo, and T. C. Hansen, *Chem. Commun.* **51**, 4180 (2015).
- ²² A. M. A. Leguy, J. M. Frost, A. P. McMahon, V. G. Sakai, W. Kochelmann, C. Law, X. Li, F. Foglia, A. Walsh, B. C. O'Regan, J. Nelson, J. T. Cabral, and P. R. F. Barnes, *Nat. Commun.* **6**, 7124 (2015).
- ²³ A. A. Bakulin, O. Selig, H. J. Bakker, Y. L. A. Rezus, C. Müller, T. Glaser, R. Lovrincic, Z. Sun, Z. Chen, A. Walsh, J. M. Frost, and T. L. C. Jansen, *J. Phys. Chem. Lett.* **6**, 3663 (2015).
- ²⁴ J. P. Perdew, A. Ruzsinszky, G. I. Csonka, O. A. Vydrov, G. E. Scuseria, L. A. Constantin, X. Zhou, and K. Burke, *Phys. Rev. Lett.* **100**, 136406 (2008).
- ²⁵ See Supplemental Material at [URL will be inserted by publisher] for an animation of the zone-centre vibrational modes of the cubic perovskite phase and a comparison of the simulated and measured diffraction patterns.
- ²⁶ A. Poglitsch and D. Weber, *J. Chem. Phys.* **87**, 6373 (1987).
- ²⁷ T. Baikie, Y. Fang, J. M. Kadro, M. Schreyer, F. Wei, S. G. Mhaisalkar, M. Gratzel, and T. J. White, *J. Mater. Chem. A* **1**, 5628 (2013).
- ²⁸ J. M. Frost, K. T. Butler, and A. Walsh, *APL Mater.* **2**, 081506 (2014).
- ²⁹ <https://github.com/WMD-Bath/Hybrid-perovskites> (Accessed 1st July 2015).
- ³⁰ R. Wasylishen, O. Knop, and J. Macdonald, *Solid State Commun.* **56**, 581 (1985).
- ³¹ Z. Fan, J. Xiao, K. Sun, L. Chen, Y. Hu, J. Ouyang, K. P. Ong, K. Zeng, and J. Wang, *J. Phys. Chem. Lett.* **6**, 1155 (2015).
- ³² C. Quarti, E. Mosconi, and F. De Angelis, *Chem. Mater.* **26**, 6557 (2014).
- ³³ R. J. Worhatch, H. J. Kim, I. P. Swainson, a. L. Yonkeu, and S. J. L. Billinge, *Chem. Mater.* **20**, 1272 (2008).
- ³⁴ F. Brivio, A. B. Walker, and A. Walsh, *APL Mater.* **1**, 042111 (2013), arXiv:1309.4215.
- ³⁵ T. Glaser, C. Müller, M. Sendner, C. Krekeler, O. E. Semonin, T. D. Hull, O. Yaffe, J. S. Owen, W. Kowalsky, A. Pucci, and R. Lovrinčić, *J. Phys. Chem. Lett.* **6**, 2913 (2015).
- ³⁶ G. Kresse and J. Furthmüller, *Comput. Mater. Sci.* **6**, 15 (1996).
- ³⁷ G. Kresse and D. Joubert, *Phys. Rev. B* **59**, 1758 (1999).
- ³⁸ P. E. Blöchl, *Phys. Rev. B* **50**, 17953 (1994).
- ³⁹ A. Togo, L. Chaput, I. Tanaka, and G. Hug, *Phys. Rev. B* **81**, 174301 (2010).
- ⁴⁰ J. M. Skelton, S. C. Parker, A. Togo, I. Tanaka, and A. Walsh, *Phys. Rev. B* **89**, 205203 (2014).
- ⁴¹ A. Togo, L. Chaput, and I. Tanaka, *Phys. Rev. B* **91**, 094306 (2015).
- ⁴² R. P. Stoffel, C. Wessel, M.-W. Lumey, and R. Dronskowski, *Angew. Chem. Int. Ed. Engl.* **49**, 5242 (2010).
- ⁴³ S. Baroni and S. D. Gironcoli, *Rev. Mod. Phys.* **73**, 515 (2001).
- ⁴⁴ J. M. Skelton, E. L. da Silva, R. Crespo-Otero, L. E. Hatcher, P. R. Raithby, S. C. Parker, and A. Walsh, *Faraday Discuss.* **177**, 181 (2015).
- ⁴⁵ M. Ledinský, P. Löper, B. Niesen, J. Holovský, S.-J. Moon, J.-H. Yum, S. De Wolf, A. Fejfar, and C. Ballif, *J. Phys. Chem. Lett.* **6**, 401 (2015).
- ⁴⁶ C. Quarti, G. Grancini, E. Mosconi, P. Bruno, J. M. Ball, M. M. Lee, H. J. Snaith, A. Petrozza, and F. D. Angelis, *J. Phys. Chem. Lett.* **5**, 279 (2014).
- ⁴⁷ T. Ahmed, C. La-o vorakiat, T. Salim, Y. M. Lam, E. E. M. Chia, and J.-X. Zhu, *Europhys. Lett.* **108**, 67015 (2014).
- ⁴⁸ J. H. Noh, S. H. Im, J. H. Heo, T. N. Mandal, and S. I. Seok, *Nano Lett.* **13**, 1764 (2013).
- ⁴⁹ J. M. Skelton, D. Tiana, S. C. Parker, A. Togo, I. Tanaka, and A. Walsh, *J. Chem. Phys.* **143**, 064710 (2015).
- ⁵⁰ N. Onoda-yamamuro, *Physico-chemical Study of Some Perovskite-type Methyl-ammonium Trihalogenometallates*, Doctoral thesis, Osaka University (1992).
- ⁵¹ Y. Fujii, S. Hoshino, Y. Yamada, and G. Shirane, *Phys. Rev. B* **9**, 4549 (1974).
- ⁵² C. Quarti, E. Mosconi, and F. De Angelis, *Phys. Chem. Chem. Phys.* **17**, 9394 (2015).
- ⁵³ M. T. Dove, *Am. Mineral.* **82**, 213 (1997).
- ⁵⁴ J. Buckeridge, D. O. Scanlon, A. Walsh, C. R. A. Catlow, and A. A. Sokol, *Phys. Rev. B* **87**, 214304 (2013).
- ⁵⁵ W. Sears, M. Klein, and J. Morrison, *Phys. Rev. B* **19**, 2305 (1979).
- ⁵⁶ E. L. Silva, J. M. Skelton, S. C. Parker, and A. Walsh, *Phys. Rev. B* **91**, 144107 (2015).
- ⁵⁷ A. Pisoni, J. Jaćimović, O. S. Barišić, M. Spina, R. Gaál, L. Forró, and E. Horváth, *J. Phys. Chem. Lett.* **5**, 2488 (2014), arXiv:1407.4931.
- ⁵⁸ Y. He and G. Galli, *Chem. Mater.* **26**, 5394 (2014).